

## Submillimeter Observations of The Isolated Massive Dense Clump IRAS 20126+4104

Hiroko Shinnaga<sup>1</sup>, Thomas G. Phillips<sup>1,2</sup>, Ray S. Furuya<sup>3</sup>, and Riccardo Cesaroni<sup>4</sup>

shinnaga@submm.caltech.edu

### ABSTRACT

We used the CSO 10.4 meter telescope to image the 350  $\mu\text{m}$  and 450 $\mu\text{m}$  continuum and CO  $J = 6 - 5$  line emission of the IRAS 20126+4104 clump. The continuum and line observations show that the clump is isolated over a 4 pc region and has a radius of  $\sim 0.5$  pc. Our analysis shows that the clump has a radial density profile  $\propto r^{-1.2}$  for  $r \lesssim 0.1$  pc and has  $\propto r^{-2.3}$  for  $r \gtrsim 0.1$  pc which suggests the inner region is infalling, while the infall wave has not yet reached the outer region. Assuming temperature gradient of  $r^{-0.35}$ , the power law indices become  $\propto r^{-0.9}$  for  $r \lesssim 0.1$  pc and  $\propto r^{-2.0}$  for  $r \gtrsim 0.1$  pc. Based on a map of the flux ratio of 350 $\mu\text{m}$ /450 $\mu\text{m}$ , we identify three distinct regions: a bipolar feature that coincides with the large scale CO bipolar outflow; a cocoon-like region that encases the bipolar feature and has a warm surface; and a cold layer outside of the cocoon region. The complex patterns of the flux ratio map indicates that the clump is no longer uniform in terms of temperature as well as dust properties. The CO emission near the systemic velocity traces the dense clump and the outer layer of the clump shows narrow line widths ( $\lesssim 3$  km s<sup>-1</sup>). The clump has a velocity gradient of  $\sim 2$  km s<sup>-1</sup>pc<sup>-1</sup>, which we interpret as due to rotation of the clump, as the equilibrium mass ( $\sim 200 M_{\odot}$ ) is comparable to the LTE mass obtained from the CO line. Over a scale of  $\sim 1$  pc, the clump rotates in the opposite sense with respect to the  $\lesssim 0.03$  pc disk associated with the (proto)star.

---

<sup>1</sup>California Institute of Technology Submillimeter Observatory (CSO) 111 Nowelo St. Hilo HI 96720

<sup>2</sup> Division of Physics, Mathematics, and Astronomy, California Institute of Technology, 1200 East California Pasadena CA 91125

<sup>3</sup>Subaru Telescope, National Astronomical Observatory of Japan, 650 N. A'ohoku Pl. Hilo HI 96720

<sup>4</sup>Osservatorio Astrofisico di Arcetri, INAF, Largo E. Fermi 5, 50125 Firenze, Italy

This is one of four objects in high-mass and low-mass star forming regions for which a discrepancy between the rotation sense of the envelope and the core has been found, suggesting that such a complex kinematics may not be unusual in star forming regions.

*Subject headings:* ISM: clouds — ISM: jets and outflows — ISM: kinematics and dynamics — ISM: lines and bands — stars: formation

## 1. INTRODUCTION

High mass star formation, especially in its earliest phase, is poorly understood because of the nature of the objects in this phase. First of all, young high mass stars are deeply embedded in their dense natal cloud cores and form and evolve on a short time scale, much shorter than that of low mass star formation. Moreover, once a massive star has reached the zero age main sequence, its strong UV radiation pressure heavily affects the surrounding material, thus making it difficult to trace back the initial conditions of the molecular cloud. Finally, high mass stars form in clusters at relatively large distances from us (typically a few kpc): it is hence not easy to resolve individual young stellar objects, even for the closest massive star forming region, Orion (e.g., Plambeck et al. 1982, Greenhill et al. 1998, Beuther et al. 2005),

The early B type massive (proto)star, IRAS 20126+4104, is a well-studied object which provides us the opportunity to study the early phase of massive star formation in a relatively simple configuration. This consists of a luminous IRAS source embedded in a dense core and associated with both a bipolar outflow and a circumstellar Keplerian disk (imaged in  $\text{NH}_3$ ,  $\text{CH}_3\text{CN}$  and  $\text{C}^{34}\text{S}$ ; Zhang et al. 1998, Cesaroni et al. 1997, 1999, 2005). The Caltech Millimeter Array (OVRO-MMA) was used to image the large scale ( $\sim 0.5$  pc) north-south outflow in detail using the CO  $J = 1 - 0$  transitions (Shepherd et al. 2000). It appears that this N–S direction is not preserved on a smaller scale (0.1 pc) where a jet oriented SE–NW has been imaged in a variety of tracers, such as shocked  $\text{H}_2$  (Cesaroni et al. 1997, Shepherd et al. 2000),  $\text{NH}_3(3,3)/(4,4)$  emission (Zhang et al. 1999), SiO and  $\text{HCO}^+$  emission (Cesaroni et al. 1997, 1999), and scattered light in the near infrared (NIR) continuum (e.g., Ayala et al. 1998, Sridharan et al. 2005). The position angle ( $PA$ ) of the jet is  $\sim 150^\circ$ , significantly different from that of the large scale molecular outflow ( $PA \simeq -25^\circ$ ; Shepherd et al. 2000, Lebrón et al. 2006). Such a discrepancy has been interpreted as precession of the jet/outflow axis (Shepherd et al. 2000, Cesaroni et al. 2005).

While many studies have been done on this object, only few of these have focused on

the dense pc-scale clump hosting the (proto)star. It is thus of interest to investigate the physical properties and evolution of such a clump and its interaction with the outflow from the (proto)star.

Here we present a study of the dense clump and bipolar outflow based on submillimeter continuum and spectroscopic observations taken with the 10.4 meter Leighton telescope at the Caltech Submillimeter Observatory (CSO)<sup>1</sup>. Note that 1.5 kpc is used as the distance of the object to estimate physical parameters in this paper. A discussion regarding the distance of this object is given in the Appendix.

## 2. OBSERVATIONS AND DATA REDUCTION

Submillimeter continuum and molecular line observations were carried out towards the massive dense clump (Table 1). The dust continuum observations at 350  $\mu\text{m}$  and 450  $\mu\text{m}$  were made on 2005 May 10 and 11 using the Submillimeter High Angular Resolution Camera II (SHARC II, Dowell et al. 2003; Voellmer et al. 2003) mounted on a Nasmyth focus. Both the 350 $\mu\text{m}$  and 450 $\mu\text{m}$  beams have simple Gaussian shapes with half-power beam widths ( $\theta_{\text{HPBW}}$ ) of 8.7'' and 9.8'' (see Table1). The 384 pixels of the bolometer array cover a region of about  $\sim 1' \times 2.6'$  at 350  $\mu\text{m}$ . Pointing and focus were checked regularly. The pointing drift due to temperature (Shinnaga 2004) was subtracted in the data reduction process. The final pointing accuracy is within  $\sim 2''$ . The Dish Surface Optimization System (DSOS) (Leong 2005) was used during the observations: this allows us to apply a gravitational deformation correction to the main mirror physically and is thus a key component for high sensitivity short submillimeter wave observations. Zenith opacities  $\tau_{225} \sim 0.06$  at the wavelength of 1300  $\mu\text{m}$  were measured with the CSO tau meter during the 350 $\mu\text{m}$  observations, while during the acquisition of the 450 $\mu\text{m}$  data we measured  $\tau_{225} \sim 0.09$ . The data were reduced with the software Comprehensive Reduction Utility (CRUSH, Kovacs 2006) version 1.41. The flux was calibrated with Neptune for both wavelengths, with an estimated calibration uncertainty of 7% at 350 $\mu\text{m}$  and 5% at 450 $\mu\text{m}$ . The estimated flux of the planet was 94.6 Jy at 350 $\mu\text{m}$  on 2005 May 10 and 55.9 Jy at 450 $\mu\text{m}$  on 2005 May 11. Note that the angular size of the planet was much smaller than the beam sizes at these wavelengths. An area of  $\sim 9'$  centered at the source position was mapped with the instrument, in box-scan mode. The RMS noise of the final maps is about 200 mJy/beam for both bands. After calibration, data analysis was done using the program GRAPHIC of the GILDAS software.

Spectroscopic observations in the CO  $J = 6 - 5$  line ( $\nu = 691.473076$  GHz, Goldsmith et

---

<sup>1</sup>The Caltech Submillimeter Observatory is supported by the NSF grant AST-0229008.

al. 1981) were made on 2004 July 8 and 9 using a 690 GHz heterodyne receiver. An area of  $2.7 \times 2.7$  was sampled with steps of  $5''$  and  $20''$ , while the innermost region of  $1' 20'' \times 1'$  was sampled with steps of  $5''$ .  $\tau_{225}$  was between 0.07 and 0.085 during the observations. The SIS receiver operation at 4K produced typical single sideband system temperatures (measured with the 1.5 GHz bandwidth Acousto-optic spectrometer) between  $\sim 7000$  K and 10900 K at 691 GHz, for elevations in the range of  $\sim 50$ – $70$  degrees. The antenna temperature  $T_A^*$  calibration was done by the standard chopper wheel method every 30 minutes to 1 hour. The data were converted to the main beam brightness temperature ( $T_{\text{mb}}$ ) scale. The  $\theta_{\text{HPBW}}$  at 691 GHz is  $\sim 10''$ . The main beam efficiency at the frequency of the CO 6–5 transition at an elevation of  $49^\circ$  was estimated to be  $\sim 40\%$ , through observations of Uranus. Pointing was checked approximately every two hours. The pointing accuracy is estimated to be  $\sim 5''$ . Daily gain variations as well as gain curve over different elevation angles were derived and corrected using CO 6–5 spectrum of NGC 7027. Frequency calibration was done every 30 minutes. The data were reduced using the program CLASS of the GILDAS software.

### 3. RESULTS AND ANALYSIS

#### 3.1. Submillimeter Dust Continuum

##### 3.1.1. Overall Structures and Flux Measurements

Submillimeter continuum observations over a 4 pc region confirmed that the object is an isolated massive dense clump (Figure 1). The submillimeter dust peak positions in both bands coincide with the 1mm and 3mm continuum peak position (RA =  $20^{\text{h}} 14^{\text{m}} 26.^{\text{s}}03$ , Decl. =  $41^\circ 13' 32.''7$  (J2000);  $l = 78^\circ 07' 20.''2$ ,  $b = 03^\circ 37' 58.''3$ ), measured by Cesaroni et al. (1999) and Shepherd et al. (2000).

The  $350\mu\text{m}$  image traces a north-south elongated single dense clump with a size of  $\sim 1.3 \times 0.7$  pc, which fits the silhouette against diffuse ionized emission. The  $450\mu\text{m}$  dust continuum, which has a size of about  $0.9 \times 0.4$  pc, looks more compact, with some extension towards the south. The clump has a prolate spheroidal shape. The effective radius of the clump is defined as  $R_{\text{eff}} = (A/\pi - \theta_{\text{HPBW}}^2/4)^{1/2}$ , where  $A$  is the area of  $2\sigma$  contour traced by  $350\mu\text{m}$  and  $450\mu\text{m}$  continuum. We find  $R_{\text{eff}350} = 0.48$  pc and  $R_{\text{eff}450} = 0.37$  pc, corresponding to angular radii of  $66''$  and  $51''$ , respectively.

The peak flux values at  $350\mu\text{m}$  and  $450\mu\text{m}$  are  $59.1 \pm 4.1$  Jy  $\text{beam}^{-1}$  and  $27.4 \pm 1.2$  Jy  $\text{beam}^{-1}$ , respectively. Within the uncertainties, these values are consistent with previous flux measurements done with SCUBA (Cesaroni et al. 1999) with  $\theta_{\text{HPBW}}=15''$ , but the  $350\mu\text{m}$

peak flux value is higher than another SHARC measurement at the same wavelength,  $34 \text{ Jy beam}^{-1}$  (Hunter et al. 2000), with  $\theta_{\text{HPBW}} = 11''$ . All peak flux densities at different wavelengths reported to date are summarized in Table 2. Our total flux densities computed inside the  $2\sigma$  contour are  $477 \pm 13 \text{ Jy}$  at  $350\mu\text{m}$  and  $137 \pm 14 \text{ Jy}$  at  $450\mu\text{m}$ , respectively.

### 3.1.2. Radial Density Profile

We approximate the column density ( $N(\text{H}_2)$ ) as a function of clump radius ( $r$ ) as a power law,  $N(\text{H}_2) \propto r^p$ . This reflects the density structure of the clump, which to a first order approximation should also scale as a power law, with index  $p - 1$ . Figure 2 represents the azimuthally averaged column density profile derived from the  $350\mu\text{m}$  data. The density profile is plotted from the clump center, i.e. the peak position at  $350\mu\text{m}$ . A discussion on the effect of a temperature gradient on the estimate of the column density profile will be given in § 4.1.

One can see that the inner part of the dense clump has a flatter index compared to that of outer part. The power law for  $0.03 \lesssim r \lesssim 0.13 \text{ pc}$  (corresponding to  $4.4''$  and  $17''$ ) is  $r^{-0.26 \pm 0.03}$ . Note that this region is larger than  $\theta_{\text{HPBW}350}/2 = 4.''3$ , so that the flatter index observed in the inner region is not due to beam dilution. In the range  $0.13 \lesssim r \lesssim 0.3 \text{ pc}$  (i.e. between  $17$  and  $40''$ ), the column density decreases as  $r^{-1.32 \pm 0.02}$ . Finally, for  $0.3 \lesssim r \lesssim 0.7 \text{ pc}$  ( $40 - 100''$ ), the index  $p$  is  $-1.98 \pm 0.02$ . Steepening of the index in this region is likely due to geometrical effects close to the clump border at  $\sim 50''$  from the center. Instead, in the two inner regions the estimates obtained are reliable and imply power law indices of  $-1.26$  and  $-2.32$  for the volume density. These issues will be further discussed in § 4.1.

### 3.1.3. $350\mu\text{m}/450\mu\text{m}$ Flux Ratio Map

The dust continuum maps taken at two different wavelengths allow us to calculate a flux ratio map. Note that such a ratio depends on two parameters: the emissivity spectral index,  $\beta$ , and the temperature of the dust grains,  $T_{\text{dust}}$ .

Figure 3 shows a map of the  $350\mu\text{m}/450\mu\text{m}$  flux ratio. Note that the  $350\mu\text{m}$  data have been smoothed to the same angular resolution as the  $450\mu\text{m}$  image. Only data above  $2\sigma$  have been used in the computation of the ratio. The plotted ratio range is between 2 and 3 in order to show the change of the ratio clearly.

The flux ratio map reveals a few intriguing features. First of all, the flux ratio towards the clump center is low ( $\sim 2$ ) and shows a bipolar structure elongated in the north-south

direction. Second, the flux ratio increases towards the outer region and reaches the maximum ( $\sim 3$ ) at  $r \sim 0.3$  pc. Such a high flux ratio is found in all directions and traces a region elongated in the north-south direction. Third, the flux ratio decreases down to  $\lesssim 2$  beyond the high flux ratio region at  $r \gtrsim 0.4$  pc.

This variation of the flux ratio can be found also in Figure 4. Here, the flux ratio is calculated over circular annuli with  $10''$  width and  $10''$  step. The error bars are the standard deviation of the ratio values measured in each annulus. Note that error of the flux ratio increases towards the clump edge, as the intensities of the continuum emission decrease.

Considering the fact that there is only one prominent heating source, the massive (proto)star, inside the dense clump, the flux ratio pattern is expected to be spherically symmetry. However, the observed pattern of the flux ratio map looks significantly elongated, which may be due to the bipolar outflow from the massive (proto)star. This will be discussed in detail in § 4.

### 3.2. Molecular Components Traced with CO Emission

We use our maps of the clump in the CO  $J = 6 - 5$  line to investigate the physical properties of the molecular gas (§ 3.2.1) as well as its low-velocity (§ 3.2.2) and high-velocity components (§ 3.2.3).

#### 3.2.1. Physical Properties Estimated From CO $J = 6 - 5$ and $J = 7 - 6$ Spectra

In Figure 5 (a), the CO  $J = 7 - 6$  spectrum (Kawamura et al 1999) is compared with the CO  $J = 6 - 5$  spectrum to infer the physical properties of the molecular gas. Figure 5 (b) shows the ratio of the main beam temperatures of these transitions. Since the temperature scale of the CO  $7 - 6$  spectrum is a lower limit (Kawamura et al. 1999), the brightness temperature ratio is to be taken as an upper limit. One can see that the red shifted wing has a higher ratio than the blue shifted one.

When dust couples well with molecular gas, the excitation temperature of the gas must be close to the temperature estimated from the spectral energy distribution (SED) of the dust continuum. Therefore line emission is expected to be optically thin when  $T_{\text{mb}}$  is lower than  $T_{\text{dust}}=T_{\text{ex}}$  ( $\sim 40$  K, Shepherd et al. 2000; see also § 4.1). Thus, the CO emission in the line wings is likely optically thin, because  $T_{\text{mb}} \ll 40$  K at high velocities.

We now wish to obtain an estimate of the gas temperature in the high velocity gas (i.e.

in the line wings) using the result in Figure 5 (b). For this purpose we express the ratio between the main beam brightness temperatures of the CO 7 – 6 and 6 – 5 lines as

$$\frac{T_{\text{mb CO 7-6}}}{T_{\text{mb CO 6-5}}} = \frac{f_{7-6}}{f_{6-5}} \cdot \left( \frac{\nu_{6-5}}{\nu_{7-6}} \right)^2 \cdot \frac{B_{\nu_{7-6}}(T_{\text{ex}}) - B_{\nu_{7-6}}(T_{\text{bg}})}{B_{\nu_{6-5}}(T_{\text{ex}}) - B_{\nu_{6-5}}(T_{\text{bg}})} \cdot \frac{1 - \exp(-\tau_{7-6})}{1 - \exp(-\tau_{6-5})} \quad (1)$$

where  $T_{\text{mb}}$  is the main beam brightness temperature of the CO transition,  $f$  is the corresponding beam filling factor, and  $B_{\nu_{J-(J-1)}}(T) = \frac{2h\nu^3}{c^2} \cdot [\exp(\frac{h\nu_{J-(J-1)}}{kT}) - 1]^{-1}$  is the Planck function. Here  $h$  and  $k$  are the Planck and Boltzmann's constants.  $T_{\text{bg}}$  is the cosmic microwave background temperature (2.7 K). At the frequencies of the CO 7 – 6 and 6 – 5 transitions ( $\nu_{7-6} = 806.652$  GHz;  $\nu_{6-5} = 691.473$  GHz),  $B_{\nu_{6-5}}(T_{\text{bg}})$  and  $B_{\nu_{7-6}}(T_{\text{bg}})$  are negligible. As already pointed out, in the line wings  $\tau \ll 1$ , so that  $[1 - \exp(-\tau)] \simeq \tau$ . Since the source is resolved, we also assume  $\frac{f_{7-6}}{f_{6-5}} \simeq 1$ . Under these approximations, the above equation can be re-written as

$$\frac{T_{\text{mb CO 7-6}}}{T_{\text{mb CO 6-5}}} \simeq \frac{\nu_{7-6}}{\nu_{6-5}} \cdot \frac{\exp\left(\frac{h\nu_{6-5}}{kT_{\text{ex}}}\right) - 1}{\exp\left(\frac{h\nu_{7-6}}{kT_{\text{ex}}}\right) - 1} \cdot \frac{\tau_{7-6}}{\tau_{6-5}} \quad (2)$$

Under local thermal equilibrium (LTE) condition, the ratio of the optical depths of the two transitions can be calculated from the following equation;

$$\frac{\tau_{7-6}}{\tau_{6-5}} \simeq \frac{\nu_{7-6}}{\nu_{6-5}} \cdot \exp\left(-\frac{h\nu_{7-6}}{kT_{\text{ex}}}\right) \cdot \frac{\exp\left(\frac{h\nu_{7-6}}{kT_{\text{ex}}}\right) - 1}{\exp\left(\frac{h\nu_{6-5}}{kT_{\text{ex}}}\right) - 1} \quad (3)$$

Substituting Equation (3) in the Equation (2), replacing  $h\nu_{7-6}/k = 38.714$  K and  $\nu_{7-6}/\nu_{6-5} = 7/6$ , and solving with respect to  $T_{\text{ex}}$ , one finds

$$T_{\text{ex}} = \frac{38.714 \text{ K}}{\ln \left[ \left( \frac{7}{6} \right)^2 \frac{T_{\text{mb CO 6-5}}}{T_{\text{mb CO 7-6}}} \right]} \quad (4)$$

Based on this equation, the blue- and red-shifted components have temperatures equal to 130 K and 30 K respectively and we thus suggest that the temperature of the blue-shifted gas is higher than that of the red-shifted gas. Please note that the difference on the ratio of the brightness temperatures of the CO lines could be partly due to difference in densities in the two outflow lobes.

We also attempted an estimate of the optical depth of these transitions using the large velocity gradient (LVG) model. Assuming an  $\text{H}_2$  volume density of  $10^5 - 10^6 \text{ cm}^{-3}$ , a CO column density of  $10^{22} - 10^{23} \text{ cm}^{-2}$ , an abundance ratio between molecular hydrogen and CO of  $10^4$  (see also § 3.2.3), and a measured line width of  $25 \text{ km s}^{-1}$ , we obtain  $\tau_{7-6} = 1.2$  and  $\tau_{6-5} = 0.7$  from the model. The tau ratio is 0.7, similar to that obtainable from Equation (3).

### 3.2.2. Narrow Line-Width Rotating Massive Dense Clump

Figure 6 shows a comparison between the  $350\mu\text{m}$  dust continuum and CO 6 – 5 line emission with LSR velocity in the range from  $-6.75$  to  $-0.25$   $\text{km s}^{-1}$ . This velocity range is chosen so that the emission in the range corresponds to the extended components.

As shown in Figure 6, the warm gas traced by the CO 6 – 5 line shows good spatial correlation with the  $350\mu\text{m}$  dust continuum emission. The molecular component traced by CO 6 – 5 is not spherically symmetric. The effective radius of the CO 6 – 5 emission,  $R_{\text{eff CO6-5}}$ , is  $0.56$  pc ( $77''$ ), larger than  $R_{\text{eff } 350}$  (§ 3.1.1). There is a strong CO 6 – 5 peak towards the clump center (i.e. the continuum peak).

The column density of the CO molecule using  $J = 6 - 5$  transition can be derived from (e.g., Equation (A1) of Scoville et al. 1986):

$$N_{\text{CO6-5}} = \frac{3k}{8\pi^3 B_{\text{CO}} \mu_{\text{CO}}^2} \cdot \frac{e^{\frac{E_{\text{CO}J=5}}{kT_{\text{ex}}}}}{6} \cdot \frac{T_{\text{ex}} + \frac{hB_{\text{CO}}}{3k}}{1 - e^{\frac{-h\nu_{\text{CO6-5}}}{kT_{\text{ex}}}}} \cdot \frac{\int T_{\text{mb}} dv}{J_{\text{CO6-5}} - J_{\text{bg6-5}}}, \quad (5)$$

where  $B_{\text{CO}}$  is the rotational constant of the molecule ( $57897.5$  MHz),  $\nu_{\text{CO6-5}}$  the frequency of the transition,  $J(T) = \frac{h\nu_{\text{CO6-5}}}{k} \frac{1}{\exp(\frac{h\nu_{\text{CO6-5}}}{kT_{\text{ex}}}) - 1}$  the specific intensity, and  $v$  is the velocity. Note that  $T_{\text{mb}} = \frac{\tau_v}{1 - e^{-\tau_v}} T_b$ , where  $T_b$  is the brightness temperature. For  $\int T_{\text{mb}} dv$ , we use an integrated spectrum of the area inside the 2 sigma contour. Since CO 7 – 6 data are available only for the central region and we don't have isotopic line data, we assume that the column density of molecular hydrogen is proportional to the observed velocity integrated  $^{12}\text{CO}$  emission,  $\int T_{\text{mb}} dv$ .

The LTE mass of the clump,  $M_{\text{LTE}}$ , is calculated as follows:

$$M_{\text{LTE}} = A \cdot N_{\text{CO6-5}} \cdot \frac{[\text{H}_2]}{[\text{CO}]} \cdot \mu_{\text{G}} \cdot m_{\text{H}_2} \quad (6)$$

with  $\frac{[\text{H}_2]}{[\text{CO}]}$  abundance ratio of molecular hydrogen to CO ( $10^4$ ),  $\mu_{\text{G}}$  mean atomic weight of the gas (1.36), and  $m_{\text{H}_2}$  mass the hydrogen molecule. The derived LTE mass is  $390 M_{\odot}$  for  $T_{\text{ex}}=40\text{K}$ . Hereafter, 40 K will be used as the temperature of the clump. Please note that the optical depth of CO 6-5 line that traces the extended clump components towards limited central region is likely to be thick. Accordingly, the LTE mass derived above is lower limit.

Figure 7 shows the LSR velocities towards selected positions where the full width at half maximum (FWHM) of the line is  $\leq 3$   $\text{km s}^{-1}$ . While the east part of the clump has LSR velocities ranging between  $\sim -1$  to  $-3.5$   $\text{km s}^{-1}$ , in the west side the velocity ranges from  $-3.0$  to  $-5.2$   $\text{km s}^{-1}$ . The velocity gradient measured over 1 pc is  $\sim 2$   $\text{km s}^{-1}\text{pc}^{-1}$ .

The rotation angular velocity,  $\Omega$ , is  $\sim 7 \times 10^{-14} \text{ s}^{-1}$ . In Figure 8 we show template spectra of the narrow line-width components observed in the east side and west side of the clump. This comparison demonstrates the clear velocity shift from east to west observed across the clump. Closely looking at the  $V_{\text{LSR}}$  change, the velocity shift might be from northeast to southwest. The direction of the velocity gradient is almost perpendicular to the major axis (directed north-south) of the massive dense clump. Assuming that the velocity shift is caused by rotation of the clump and that centrifugal forces balance gravitational ones, one can estimate the equilibrium mass of the molecular dense clump as  $M_{\text{rot}} \simeq \frac{\Omega^2 \cdot r^3}{G} = 200 M_{\odot}$ , where  $G$  is the gravitational constant. This value agrees reasonably well with the LTE mass, supporting the idea that the velocity gradient may be largely due to rotation of the clump.

We note that rotation of the narrow line-width molecular gas component occurs in the opposite sense with respect to rotation of the circumstellar Keplerian disk associated with the (proto)star. A similar discrepancy in the sense of rotation on different spatial scales, has been observed also in W3 (Hayashi et al. 1989) and Orion (Harris et al. 1983), for massive star forming regions, and in a starless core, L1521F (MC27) in the Taurus Molecular Cloud (Shinnaga et al. 2004), for low-mass star forming regions. This suggests that such a complex kinematical structure may not be unusual in the star formation process.

The measured  $\Delta v_{\text{FWHM}}$  averaged over the entire CO 6 – 5 emitting region is  $3.9 \pm 0.2 \text{ km s}^{-1}$ . From the line width, one can derive the virial mass,  $M_{\text{VIR}}$ , of the clump:

$$M_{\text{VIR}} \sim \frac{5 + 2e}{3 + e} \cdot \frac{R_{\text{eff CO6-5}}}{G} \sigma_{v_{\text{total}}}^2 \quad . \quad (7)$$

where the volume density is proportional to  $r^{-e}$ . The virial mass is estimated to be  $400 M_{\odot}$  for this dense clump. One can assess the equilibrium of the dense clump by comparing this value with the LTE mass and the one obtained assuming centrifugal equilibrium. We note that  $M_{\text{LTE}} \simeq M_{\text{rot}}$  and at the same time,  $M_{\text{LTE}} \simeq M_{\text{VIR}}$ . This suggests that the clump is in an equilibrium state and rotation of the core contributes significantly to the equilibrium of the clump.

Figure 9 shows the non-thermal velocity dispersion,  $\sigma_{v_{\text{nt}}}$ , of the narrow line-width molecular gas components. Note that the diagram of the velocity width is plotted under an assumption of constant temperature over the core. Since the optical depth of the CO 6 – 5 line is relatively small (see § 3.2.1), one can estimate the non-thermal velocity dispersion ( $\sigma_{v_{\text{nt}}}$ ) by subtracting the thermal line width ( $\frac{kT_{\text{k}}}{m_{\text{avr}}}$ )<sup>1/2</sup> from total velocity dispersion,  $\sigma_{v_{\text{total}}} = [\sigma_{v_{\text{obs}}}^2 - kT_{\text{k}}(\frac{1}{m_{\text{CO}}} - \frac{1}{m_{\text{avr}}})]^{1/2}$ , where  $\sigma_{v_{\text{obs}}}$  is the observed velocity dispersion,  $m_{\text{avr}}$  is the average mass unit, and  $m_{\text{CO}} = 28 \text{ amu}$  is the mass of the CO molecule.  $\sigma_{v_{\text{obs}}}$  can be expressed as  $\Delta v_{\text{FWHM}}(4 \ln 2)^{-1/2}$ , where  $\Delta v_{\text{FWHM}}$  is the observed line FWHM. From Figure 10, one can see that the non-thermal velocity dispersion decreases with increasing distance from

the clump center. To derive the non-thermal velocity dispersion, 40 K has been used as gas kinetic temperature. The dotted line in the diagram shows the thermal velocity dispersion when  $T_k = 40$  K. One can see that the thermal velocity dispersion becomes dominant at  $r = 0.6$  pc ( $\sim 80''$ ).

### 3.2.3. CO 6 – 5 Large Scale Bipolar Outflow

Figure 11 shows the CO  $J = 6 - 5$  spectra taken towards three positions and the mean spectrum over a  $\leq 120''$  area around the clump center. One can see prominent wings in the spectra taken towards each outflow lobe. Blue- and red-shifted emission is detected over the velocity ranges  $-34.0 \leq V_{\text{LSR}} \text{ km s}^{-1} \leq -6.0$  and  $0.0 \leq V_{\text{LSR}} \text{ km s}^{-1} \leq +30$ , respectively. The spectrum observed towards the clump center ( $0'', 0''$ ) and the mean spectrum clearly show both red- and blue-shifted emission. The spectrum taken towards the center position has a strong peak at  $V_{\text{LSR}} = -3 \text{ km s}^{-1}$ .

Figure 12 shows the distribution of CO  $J = 6 - 5$  blue-shifted and red-shifted emission superposed on the  $350\mu\text{m}$  dust continuum emission map. Both outflow lobes are located inside the  $350\mu\text{m}$  dust continuum component. The red-shifted bipolar outflow lobe is more than twice extended compared with the blue-shifted outflow lobe. Integrated intensities of the blue- and red-shifted outflow lobes are measured to be  $(9.6 \pm 0.9) \times 10^2$  and  $\gtrsim (2.5 \pm 0.1) \times 10^3 \text{ K km s}^{-1}$ , respectively. The masses of the blue and red shifted outflows are estimated to be 28 and 13  $M_\odot$ , respectively. From the outflow velocity,  $\sim 30 \text{ km s}^{-1}$ , and the extension of the outflow,  $\sim 0.6$  pc, one can estimate the dynamical time scale of the bipolar outflow. The averaged dynamical time scale of the outflow is estimated to be  $\gtrsim 1.7 \times 10^4$  years. Note that the estimated age is lower limit because the south edge of the red shifted outflow lobe isn't fully covered and the inclination angle is unknown. The inclination angle affects the size and velocity. The outflow parameters derived from the CO 6 – 5 and 1 – 0 lines are summarized in Table 3. The outflow velocities obtained from the 6 – 5 line are higher than those from the 1 – 0, while the mean dynamical time scale of the 6 – 5 flow is shorter than that of the 1 – 0. A more detailed discussion of the outflow properties will be given in § 4.

## 4. DISCUSSION

### 4.1. Dust Property and Column Density Profile

To derive the dust mass  $M_{\text{dust}}$ , we have used the expression (see Hildebrand 1983),

$$M_{\text{dust}} = \frac{F_{\nu} D^2}{B_{\nu}(T_{\text{dust}})} \cdot \frac{1}{\kappa_{\nu}}, \quad (8)$$

where  $F_{\nu}$  is the measured flux density,  $D$  the distance to the object, and  $B_{\nu}(T_{\text{dust}})$  the Planck function. The coefficient  $1/\kappa_{\nu}$  ( $\kappa_{\nu}$  is dust opacity), is estimated to be  $0.1 \text{ g} \cdot \text{cm}^{-2}$  at  $250\mu\text{m}$  in NGC7023 (Hildebrand 1983).  $\kappa_{\nu}$  depends on the frequency as  $\kappa_{\nu} \propto \nu^{\beta}$ .  $\beta$  may range from  $\sim 1$  at  $\lambda \lesssim 200\mu\text{m}$  to  $\gtrsim 2$  at  $\sim 1 \text{ mm}$  (Hildebrand 1983 and the references therein). Extrapolating  $\kappa_{\nu}$  from  $250\mu\text{m}$  to  $350\mu\text{m}$ , one obtains  $\kappa_{850\text{GHz}} \simeq 5.6 \text{ cm}^2 \text{ g}^{-1}$ .  $\beta$  can be estimated from the flux ratio of  $350\mu\text{m}$  and  $450\mu\text{m}$  using the equation

$$\frac{F_{\nu_1}}{F_{\nu_2}} \cdot \frac{\Omega_{\nu_1}}{\Omega_{\nu_2}} = \frac{B_{\nu_2}(T_{\text{dust}})}{B_{\nu_1}(T_{\text{dust}})} \cdot \left( \frac{\nu_1}{\nu_2} \right)^{\beta}, \quad (9)$$

where  $\Omega_{\nu}$  is the beam solid angle. Note that in our case  $\frac{\Omega_{\nu_1}}{\Omega_{\nu_2}} \simeq 1$ , because the  $350\mu\text{m}$  image has been smoothed to the same angular resolution as the  $450\mu\text{m}$  image.

Assuming that the clump mass equals  $M_{\text{rot}} \simeq 200 M_{\odot}$ , one may use Equation (8) to derive an estimate of the mean clump temperature,  $T_{\text{dust}} = 40 \text{ K}$ . Then Equation (9) gives  $\beta \simeq 1.7$ . This value lies within the typical range  $1.5 \lesssim \beta \lesssim 2.4$  for high mass star forming regions (e.g., Molinari et al. 2000). The dust temperature is more or less consistent with the temperature,  $\sim 44 \text{ K}$ , derived from the SED fitting by Shepherd et al. (2000), but lower than the  $60 \text{ K}$  estimated by Cesaroni et al. (1999). Note that the errors on  $\beta$  and especially  $T_{\text{dust}}$  may be significant, as  $M_{\text{rot}}$  ( $200 M_{\odot}$ ) might not represent the true clump mass. Hofner et al. (2007) estimates a clump mass of  $\sim 400 M_{\odot}$  from their SED fitting. The column density towards the clump center is estimated to be  $\sim 3.4 \times 10^{23} \text{ cm}^{-2}$ , using the values of  $\beta$  and  $T_{\text{dust}}$  described above. This implies a volume density of  $\sim 10^6 \text{ cm}^{-3}$  towards the clump center. Towards the outflow lobes, the estimated number density becomes  $\sim 10^5 \text{ cm}^{-3}$ .

A temperature gradient is likely to exist inside the clump, as this is internally heated by the embedded (proto)star. Such a gradient is likely to be similar to a power law of the type  $T(r) \propto r^{-2/(4+\beta)}$  (Doty & Leung 1994), with  $r$  distance from the clump center. In our case  $\beta = 1.7$  and hence the the power law index is  $-0.35$ . The effect of this gradient on the estimated density slopes inside the clump is to change the power law indices of the inner ( $0.13 \lesssim r \lesssim 0.3 \text{ pc}$ ) and outer ( $0.3 \lesssim r \lesssim 0.7 \text{ pc}$ ) regions to  $\sim -0.9$  and  $\sim -2$ ,

respectively. This has been assessed by recalculating the column density profile assuming the clump is spherically symmetric. These indices are not significantly different from those derived without taking the temperature gradient into account. For the non-thermal velocity dispersion described in § 3.2.2, the velocity dispersion won't change much (order of 0.01 km s<sup>-1</sup>) even when we consider an temperature gradient of  $T(r) \propto r^{-0.35}$ .

An index of  $-1.26$  for the  $0.03 \lesssim r \lesssim 0.13$  pc region is only slightly shallower than that typical of a region undergoing free-fall ( $\rho(r) \propto r^{-\frac{3}{2}}$ ) – as in the runaway collapse model (Larson-Penston-Hunter solution, Larson 1969; Penston 1969; Hunter 1977) and the inside-out collapse model by Shu et al. (1987). Instead, an index of  $-2.32$  for the  $0.13 \lesssim r \lesssim 0.3$  pc region resembles the density profile  $\rho(r) \propto r^{-2}$  of a system in hydrostatic equilibrium. We thus speculate that the inner region of the clump is experiencing infall, whereas the “infalling wave” has not yet reached the outer region beyond  $r \gtrsim 0.1$  pc.

## 4.2. Internal Structures of The Dense Clump

### 4.2.1. CO 6 – 5 Outflow and Shocked H<sub>2</sub> Knots

From Figure 12, one can see a spatial coincidence between the outflow lobes and the shocked H<sub>2</sub> knots. All six knots lie inside the CO 6–5 bipolar outflow lobes. More specifically, the CO 6 – 5 emission shows clear peaks close to the H2-5 and H2-6 knots located in the red shifted lobe. Such a correlation between CO 6 – 5 peaks and shocked H<sub>2</sub> knots indicates that they are physically associated. Note that, unlike the CO 6 – 5 emission, no peak towards the knot positions is found in the CO 1 – 0 line, as one can see in Figure 1 of Shepherd et al. (2000). A likely interpretation is that CO 6 – 5 traces more excited gas compared to the 1 – 0 transition. This might be due to the gas at the knot locations being heated and compressed by interaction with the jet powered by the (proto)star.

### 4.2.2. Implications from the Submillimeter Dust Radio Map

There are three major components in the submillimeter flux ratio map (see § 3.1.3 and Figure 3), namely: (1) a bipolar feature in the central region of the clump, with flux ratio  $\simeq 2 - 2.2$ ; (2) a region  $\sim 0.5$  pc in diameter and elongated north-south, with flux ratio starting from  $\sim 2 - 3$  and increasing upto  $\gtrsim 3$  close to the outer border; and (3) region of lower flux ratio,  $\lesssim 2$ , outside of component (2). Component (1) is located inside component (2). The *PA* of the bipolar structure is about  $-17^\circ$ . Note that features (1) and (2) are detected above a  $3\sigma$  level in the 450  $\mu\text{m}$  map and above a  $5\sigma$  level in the 350  $\mu\text{m}$  map. Note

that  $450\mu\text{m}$  emission in component (3) is detected at a  $2 - 3\sigma$  level, whereas the  $350\mu\text{m}$  emission is much stronger. Therefore, we believe that all the three features represent real structures.

Equation (9) shows that the ratio between the  $350$  and  $450\mu\text{m}$  fluxes is an increasing function of both  $\beta$  and (albeit more weakly)  $T_{\text{dust}}$ . It is thus impossible to decide whether a change in the ratio is due to a variation of  $\beta$ , temperature, or both. For example, for  $T = 40$  K, a  $\beta$  of 1 and 2 implies a flux ratio of 1.9 and 2.4, respectively. Vice versa, for  $\beta=1.7$ , a temperature of 20, 40, and 60 K implies a flux ratio of 1.9, 2.3, and 2.4, respectively. From these numbers one can see that, in order to reproduce flux ratios as large ( $\sim 3$ ) as those measured on the surface of component (2), very likely an increase of both  $\beta$  and  $T_{\text{dust}}$  is needed. Hence component (2), which encases the bipolar feature, might be a cocoon of dense material with warm surface. On the other hand, the lower flux ratio value of component (3) indicates that  $T_{\text{dust}}$  and/or  $\beta$  in the region ahead of the outflow lobes are lower compared to component (2). We speculate that the higher  $T_{\text{dust}}$  and  $\beta$  observed on the surface of the cocoon represented by component (2) might be due to a weak shock, propagating from the (proto)star and possibly created by the outflow. Considering a sound speed of  $\sim 0.8$  km s $^{-1}$ , the crossing time of the weak shock would be  $\lesssim 3 \times 10^5$  years. Note that this is likely an upper limit to the age of the outflow (and perhaps of the (proto)star), as shock waves may propagate with larger velocities than the sound speed.

How to explain the low flux ratio in component (1)? The fact that the shape of this region matches very well the outflow lobes suggests a connection between the two. This suggests that the flow might have swept away the smallest grains from that region, thus biasing the grain size towards the largest ones. This phenomenon would have the effect of reducing the slope of the spectral index  $\beta$  and hence of the flux ratio.

In conclusion, the flux ratio variations across the clump strongly suggest that the massive dense clump is no longer uniform in terms of temperature as well as dust properties. To construct a model to explain the observed features, one must keep in mind such inhomogeneities.

#### 4.2.3. Comparison Between Submillimeter Flux Ratio Map And Molecular Components

Here we make a detailed comparison between the flux ratio map and the structure of the dense clump and outflow. Figure 13 shows the CO 6 – 5 and CO 1 – 0 outflow lobes superposed on the flux ratio map. We have already discussed the good correlation between the CO outflow and the bipolar component (1) of the flux ratio map. Now, we note also

that the peak of the blue shifted CO 6–5 lobe is located on the west edge of the northern bipolar feature, which may be due to interaction with the jet detected in SiO and H<sub>2</sub> line emission (Cesaroni et al. 1999) and oriented with  $PA \simeq -60^\circ$ . This jet might have excited the molecular gas lying on the west side of the northern lobe. Nothing similar is seen to the SW in correspondence to the CO 6 – 5 red shifted outflow lobe. There are two distinct CO 6 – 5 red shifted peaks associated with the shocked H<sub>2</sub> knots, H2-5 and -6, located at (14'', -30'') and (17'', -48'') respectively, as described in § 4.2.1. At the position of the H2-5 knot, a high value of the flux ratio ( $\sim 3$ ) is observed, suggesting relatively large values for both the temperature and  $\beta$ . In correspondence to the CO 6 – 5 peak associated with knot H2-6, the flux ratio is  $\lesssim 2.5$ . The difference in flux ratio between H2-5 and H2-6 may indicate that the temperature and/or  $\beta$  at the position of knot H2-6 could be lower than those of H2-5.

## 5. SUMMARY

An observational study of the IRAS 20126+4104 clump is presented. The main findings of this study are summarized as follows.

(I) The 350 $\mu$ m and 450 $\mu$ m dust continuum images revealed that the power law index of the volume density in the inner part of the clump is  $-1.26 \pm 0.03$  ( $r \leq 0.1$  pc), shallower than that in the outer part,  $-2.32 \pm 0.02$  ( $0.3 \leq r \leq 0.1$  pc). The power law indices suggest that the inner region might be infalling, while the outer region of the clump is still in hydrostatic equilibrium.

(II) A map of the peak velocity of narrow line-width CO 6–5 components reveals a velocity gradient across the clump, suggesting rotation about an axis oriented northwest–southeast. The rotation occurs in the opposite sense with respect to the circumstellar Keplerian disk associated with the massive (proto)star.

(III) Assuming centrifugal equilibrium, one estimates an enclosed mass  $M_{\text{rot}}$  of  $\sim 200M_\odot$ . Estimated  $M_{\text{LTE}}$  and  $M_{\text{VIR}}$  ( $\sim 400M_\odot$ ) of the clump are comparable to  $M_{\text{rot}}$ . This indicates that the clump is in equilibrium state as a whole and rotation contributes a large fraction to support the clump from gravitational collapse on large clump scale. At the radius of 0.1 pc, the rotation may be disconnected from the inner region and the medium inside of  $r \sim 0.1$  pc may be infalling. This might be partly related to the disagreement of the rotational axes of the large scale clump and of the disk associated with the massive (proto)star.

(IV) The mean spectral index  $\beta$  and dust temperature are estimated to be 1.7 and 40 K, respectively.

(V) The  $350\mu\text{m}/450\mu\text{m}$  ratio map outlines three major components, namely: (1) a bipolar feature, which may represent the region swept by the bipolar outflow lobes; (2) a dense cocoon  $\sim 0.5$  pc in diameter, with a warm surface; and (3) a low temperature/low  $\beta$  component outside component (2). These three components indicate that the temperature as well as the nature of the dust (grain size distribution and composition) may vary significantly inside the dense clump. The warm layer of component (2) might have been created by a shock propagating from the (proto)star. The crossing time of the shock is estimated to be  $\gtrsim 3 \times 10^5$  years.

(VI) Strong correlation between CO 6 – 5 peaks and two of the shocked H<sub>2</sub> knots are identified, indicating they are physically associated.

This research was performed at the Caltech Submillimeter Observatory, supported by NSF grant AST-0229008. HS is grateful to Hiroshige Yoshida for the observational support in July 2004 and Debra Shepherd and J. H. Kawamura for providing us their data. HS is indebt to Dr. Peter Schilke for his LVG code. Thanks are also due to Thomas A. Bell, John Carpenter and Roger Hildebrand for valuable comments and discussions. HS also thank the Gildas development team (<http://www.iram.fr/IRAMFR/GILDAS>) which provides us their data reduction packages. We thank the Hawaiian people for allowing us to observe from the summit of their sacred mountain, Maunakea.

Facilities: CSO

### A. Appendix: Distance To The Massive Dense Clump

IRAS 20126+4104 is located in the northwest side of the Cygnus X region. This region (Piddington & Minnett 1952; Davies 1957) is one of the most active star forming complexes in the Galaxy. Here one can find a large variety of objects, including OB associations, atomic diffuse clouds, molecular dense clouds/cores, evolved stars, and supernova remnants. The distance of the massive dense clump under study is not well established as it lies on the tangential direction of the spiral arm or bridge structure to which the Sun belongs in our Galaxy (Sharpless 1965; Kerr & Westerhout 1965). Many studies reporting on observations of IRAS 20126+4104 adopt a distance of 1.7 kpc, based on the value quoted by Dame & Thaddeus (1985). However, Dame & Thaddeus (1985) do not explain how such a distance was derived. The kinematical estimate using a galactic rotation model may not be accurate for this source because of the location of the source relative to the Galactic Center. An alternative method is that of looking for a possible interaction of the IRAS 20126+4104 clump with nearby objects whose distances are known. From the north-east to the north of the source, there is

a chain of HII regions, whose northern edge coincides with IC1318a, the biggest HII region in the cluster. IRAS 20126+4104 is located close to the south-western edge of the chain. The angular distance from the closest HII region is about  $7'$ . In addition, there is a number of HII regions to the east of the source and one supernova remnant (SNR), G 78.2+2.1 (Higgs et al. 1977; Landecker et al. 1980) with diameter of  $\sim 62''$  to the south-east of it. The angular distance between the dense clump and the supernova remnant is about  $1.5^\circ$ , along a direction with  $PA \sim 120^\circ$ . To the south-east of the object, there is an O star, HD193322 (O9V). The angular separation between HD193322 and IRAS 20126+4104 is about  $51'$ . The distance of the O star is estimated to be  $\sim 1$  kpc from photometry (Cruz-Gonzalez et al. 1974). To the south-west, there is no strong HII region. Ionized gas appears to surround the massive dense clump except on the south-west side, as shown in Figure 1 (§ 3.1), which is evidence of interaction between our clump and all these objects. The ionized gas is likely due to irradiation from these HII regions and from the SNR. As the distance of these sources is reported to be  $1.5 \pm 0.5$  kpc (Iksanov 1960, Dickel et al. 1969, Higgs et al. 1977, Landecker et al. 1980, Piepenbrink & Wendker 1988, and references therein), in this paper we assume a distance of 1.5 kpc for IRAS 20126+4104.

## REFERENCES

- Ayala, S., Curiel, S., Raga, A. C., Noriega-Crespo, A., & Salas, L. 1998, *A&A*, 332, 1055
- Beuther, H., Schilke, P., Menten, K. M., Motte, F., Sridharan, T. K., & Wyrowski, F. 2002, *ApJ*, 566, 945
- Beuther, H., et al. 2005, *ArXiv Astrophysics e-prints*, arXiv:astro-ph/0506603
- Cesaroni, R., Felli, M., Testi, L., Walmsley, C. M., & Olmi, L. 1997, *A&A*, 325, 725
- Cesaroni, R., Felli, M., Jenness, T., Neri, R., Olmi, L., Robberto, M., Testi, L., & Walmsley, C. M. 1999, *A&A*, 345, 949
- Cesaroni, R., Neri, R., Olmi, L., Testi, L., Walmsley, C. M., & Hofner, P. 2005, *A&A*, 434, 1039
- Cruz-Gonzalez, C., Recillas-Cruz, E., Costero, R., Peimbert, M., & Torres-Peimbeert, S. 1974, *Revista Mexicana de Astronomia y Astrofisica*, 1, 211
- Dame, T. M., & Thaddeus, P. 1985, *ApJ*, 297, 751
- Davies, R. D. 1957, *MNRAS*, 117, 663

- Dickel, H. R., Wendker, H. J., & Bieritz, J. H. 1969, *A&A*, 1, 270
- Doty, S. D., & Leung, C. M. 1994, *ApJ*, 424, 729
- Dowell, C. D., et al. 2003, *Proc. SPIE*, 4855, 73
- Fontani, F., Cesaroni, R., Caselli, P., & Olmi, L. 2002, *A&A*, 389, 603
- Greenhill, L. J., Gwinn, C. R., Schwartz, C., Moran, J. M., & Diamond, P. J. 1998, *Nature*, 396, 650
- Harris, A., Townes, C. H., Matsakis, D. N., & Palmer, P. 1983, *ApJ*, 265, L63
- Hayashi, M., Kobayashi, H., & Hasegawa, T. 1989, *ApJ*, 340, 298
- Higgs, L. A., Landecker, T. L., & Roger, R. S. 1977, *AJ*, 82, 718
- Hildebrand, R. H. 1983, *QJRAS*, 24, 267
- Hofner, P., Cesaroni, R., Olmi, L., Rodríguez, L. F., Martí, J., & Araya, E. 2007, *A&A*, 465, 197
- Hunter, C. 1977, *ApJ*, 218, 834
- Hunter, T. R., Churchwell, E., Watson, C., Cox, P., Benford, D. J., & Roelfsema, P. R. 2000, *AJ*, 119, 2711
- Ikhsanov, R. N. 1960, *Soviet Astronomy*, 4, 258
- Kawamura, J. H., Hunter, T. R., Tong, C.-Y. E., Blundell, R., Zhang, Q., Katz, C. A., Papa, D. C., & Sridharan, T. K. 1999, *PASP*, 111, 1088
- Kerr, F.J. and Westerhout, G. 1965, in *Galactic Structure*, ed. A. Blaauw and M. Schmidt, Chicago Univ. of Chicago Press 167
- Kovacs, A. 2005 Ph.D. thesis at California Institute of Technology
- Landecker, T. L., Roger, R. S., & Higgs, L. A. 1980, *A&AS*, 39, 133
- Larson, R. B. 1969, *MNRAS*, 145, 271
- Lasker, B. M., Sturch, C. R., McLean, B. J., Russell, J. L., Jenkner, H., & Shara, M. M. 1990, *AJ*, 99, 2019
- Leong M. M. 2005, *URSI Conf. Sec. J3-10*, 426, <http://astro.uchicago.edu/ursi-comm-J/ursi2005/rf-telescope-fabrication/leong>

- Lebrón, M., Beuther, H., Schilke, P., & Stanke, T. 2006, *A&A*, 448, 1037
- Molinari, S., Brand, J., Cesaroni, R., & Palla, F. 2000, *A&A*, 355, 617
- Penston, M. V. 1969, *MNRAS*, 144, 425
- Piddington, J. H., & Minnett, H. C. 1952, *Aust. J. Sci. Res.* A5, 17
- Piepenbrink, A., & Wendker, H. J. 1988, *A&A*, 191, 313
- Plambeck, R. L., Wright, M. C. H., Welch, W. J., Bieging, J. H., Baud, B., Ho, P. T. P., & Vogel, S. N. 1982, *ApJ*, 259, 617
- Scoville, N. Z., Sargent, A. I., Sanders, D. B., Claussen, M. J., Masson, C. R., Lo, K. Y., & Phillips, T. G. 1986, *ApJ*, 303, 416
- Sharpless, S. 1965, in *Galactic Structure*, ed. A. Blaauw and M. Schmidt, Chicago Univ. of Chicago Press 131
- Shepherd, D. S., Yu, K. C., Bally, J., & Testi, L. 2000, *ApJ*, 535, 833
- Shinnaga, H., Ohashi, N., Lee, S.-W., & Moriarty-Schieven, G. H. 2004, *ApJ*, 601, 962
- Shinnaga, H. 2004, Technical Memorandum at The Caltech Submillimeter Observatory available on a web at [http://www.submm.caltech.edu/~sim\\$hs/memo/shinnaga-memo04nov.ps](http://www.submm.caltech.edu/~sim$hs/memo/shinnaga-memo04nov.ps)
- Shu, F. H., Adams, F. C., & Lizano, S. 1987, *araa*, 25, 23
- Sridharan, T. K., Williams, S. J., & Fuller, G. A. 2005, *ArXiv Astrophysics e-prints*, arXiv:astro-ph/0508342
- Voellmer, G. M., et al. 2003, *Proc. SPIE*, 4855, 63
- Williams, S. J., Fuller, G. A., & Sridharan, T. K. 2004, *A&A*, 417, 115
- Zhang, Q., Hunter, T. R., & Sridharan, T. K. 1998, *ApJ*, 505, L151
- Zhang, Q., Hunter, T. R., Sridharan, T. K., & Cesaroni, R. 1999, *ApJ*, 527, L117

Table 1. Observations

Emission	Frequency (GHz)	Bandwidth (MHz)	Telescope/ Instrument	$\theta_{\text{HPBW}}^{\text{a}}$ ( $''$ )	FOV <sup>b</sup> (arcmin <sup>2</sup> )	Velocity resolution (kms <sup>-1</sup> )	Reference
350 $\mu\text{m}$ continuum	849.4	102900	CSO/SHARC II	8.7	9 $\times$ 9	...	This work
450 $\mu\text{m}$ continuum	658.3	67900	CSO/SHARC II	9.8	9 $\times$ 9	...	This work
CO $J = 6 - 5$	691.473076	50	CSO/690GHz Rx	10	2.7 $\times$ 2.7	0.6	This work
CO $J = 7 - 6$	806.651776	250	HHT <sup>c</sup> /800GHz Rx	10	...	0.9	Kawamura et al. (1999)

<sup>a</sup>Half power beam width.

<sup>b</sup>Field of view.

<sup>c</sup>The Heinrich Hertz Telescope.

<sup>d</sup>The largest angular scale detected with the interferometric observations = 16 $''$ .

Table 2. Peak Flux Densities and Total Flux

Wavelengths ( $\mu\text{m}$ )	Telescope/ Instrument	$\theta_{\text{HPBW}}^{\text{a}}$ (")	Flux density <sup>b</sup> (Jy Beam <sup>-1</sup> )	Total flux <sup>b</sup> (Jy)	Effective radius (")	Reference
350	CSO/SHARC II	8.7	59.1 (4.1)	477 (13)	65.5	This work
350	CSO/SHARC	11	34	130	25	Hunter et al. (2000)
450	CSO/SHARC II	9.8	27.4 (1.2)	137 (14)	50.4	This work
450	JCMT/SCUBA	8	29 (0.9)	91.1(3.9)	...	Williams et al. (2004)
450	JCMT/SCUBA	12	32.0 (6.0)	162 (24)	...	Cesaroni et al. (1999)
850	JCMT/SCUBA	14.4	5.6 (0.04)	21.9 (0.5)	15	Williams et al. (2004)
850	JCMT/SCUBA	21	5.3 (0.6)	19 (3)	...	Cesaroni et al. (1999)
1200	Pico Veleta/MAMBO	11	1.1 (0.3)	5.8	20	Beuther et al. (2002)
1350	JCMT/SCUBA	22	1.74 (0.20)	...	...	Cesaroni et al. (1999)
2000	JCMT/SCUBA	33	0.56 (0.05)	...	...	Cesaroni et al. (1999)

<sup>a</sup>Half power beam width.

<sup>b</sup>Error is given in the parenthesis when the literatures provide.

Table 3. IRAS 20126+4104 CO Outflow Parameters

Transition	$l^a$		$M^b$		$PA$	$V^c$		$\tau_{\text{dyn}}$	Reference
	Red (pc)	Blue (pc)	Red ( $M_{\odot}$ )	Blue ( $M_{\odot}$ )		Red ( $\text{km s}^{-1}$ )	Blue ( $\text{km s}^{-1}$ )		
$J = 6 - 5$	0.23	0.16	13	28	50	35	30	$\gtrsim 1.7 \times 10^4$	This work
$J = 1 - 0$	0.64	0.35	20	33	-10	25	> 28	$6.4 \times 10^4$	Shepherd et al. (2000)

<sup>a</sup>Outflow lobe radius.

<sup>b</sup>Mass of the outflow lobes.

<sup>c</sup>Outer boundary of the wing components.

<sup>d</sup>Dynamical timescale.

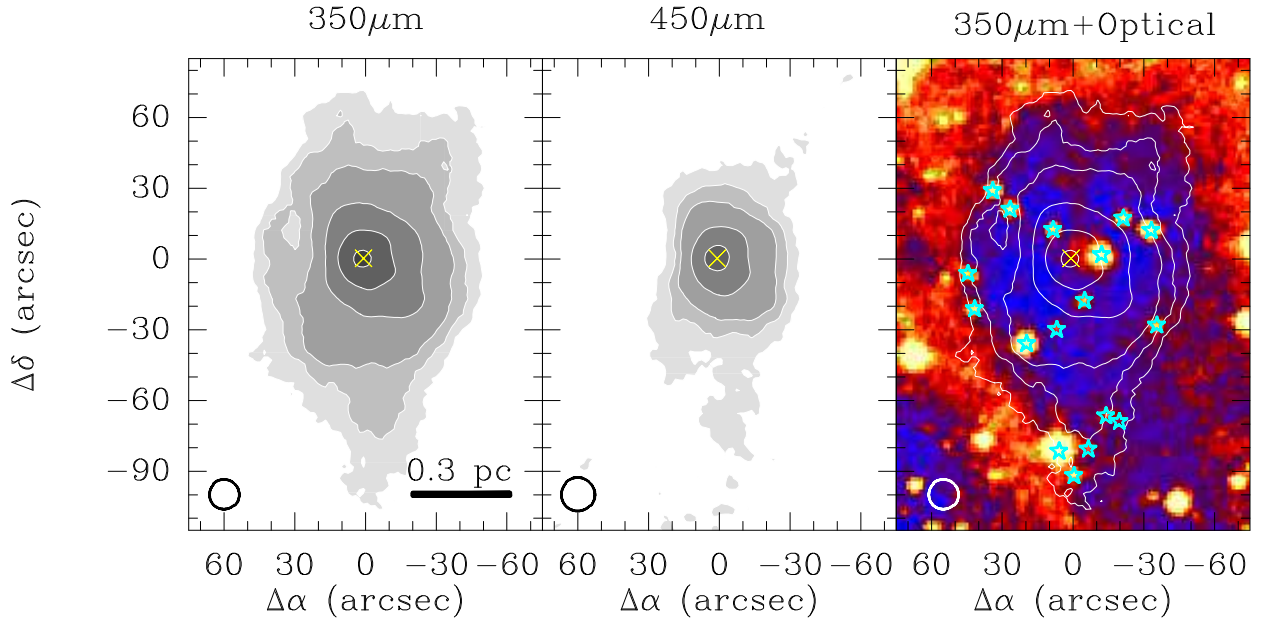


Fig. 1.— SHARC II  $350\mu\text{m}$  (left panel)  $450\mu\text{m}$  (middle panel) images of the dense clump. The  $350\mu\text{m}$  image is overlaid on the optical image (DSS  $0.5\mu\text{m}$ , color) in the right panel. Blue stars mark the positions of foreground stars. Grey scale contours of two images from left are drawn at  $2\sigma$ ,  $5\sigma$ ,  $9\sigma$ ,  $27\sigma$ ,  $81\sigma$ , and  $243\sigma$ , where  $1\sigma=200\text{ mJy beam}^{-1}$ . The yellow cross at the center represents the position of the clump center, namely the peak of the  $350\mu\text{m}$  continuum emission. The beams is shown in the left bottom corner of each panel.

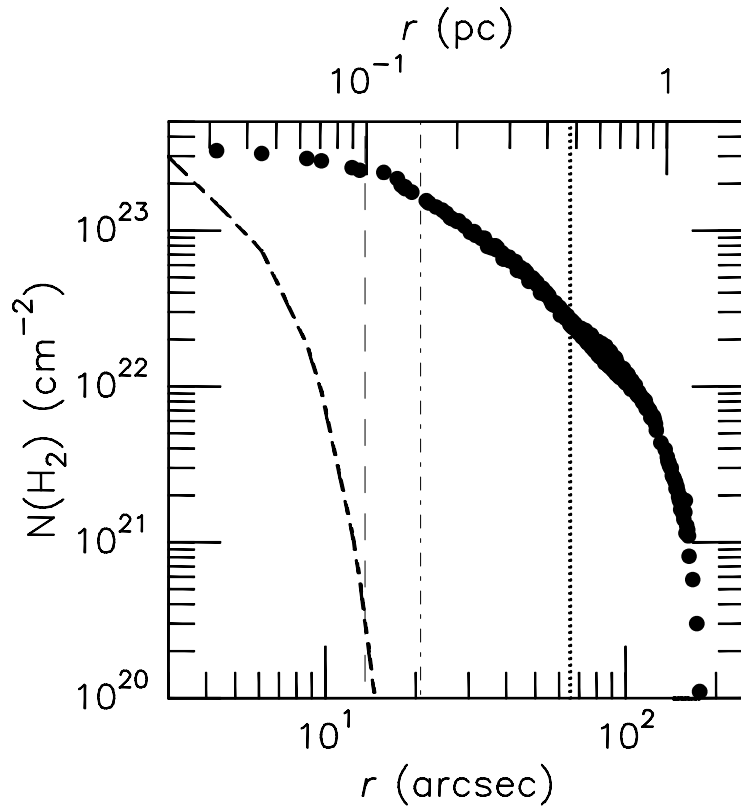


Fig. 2.— Radial column density profile of the dense clump (black dots) derived using the  $350\mu\text{m}$  data. The thick broken line represents the beam shape. The vertical dotted line marks  $R_{\text{eff}350}$ . The dash-dotted and long-dashed lines mark the effective radii of the continuum emission measured at  $1.2\text{mm}$  and at  $850\mu\text{m}$ , respectively.

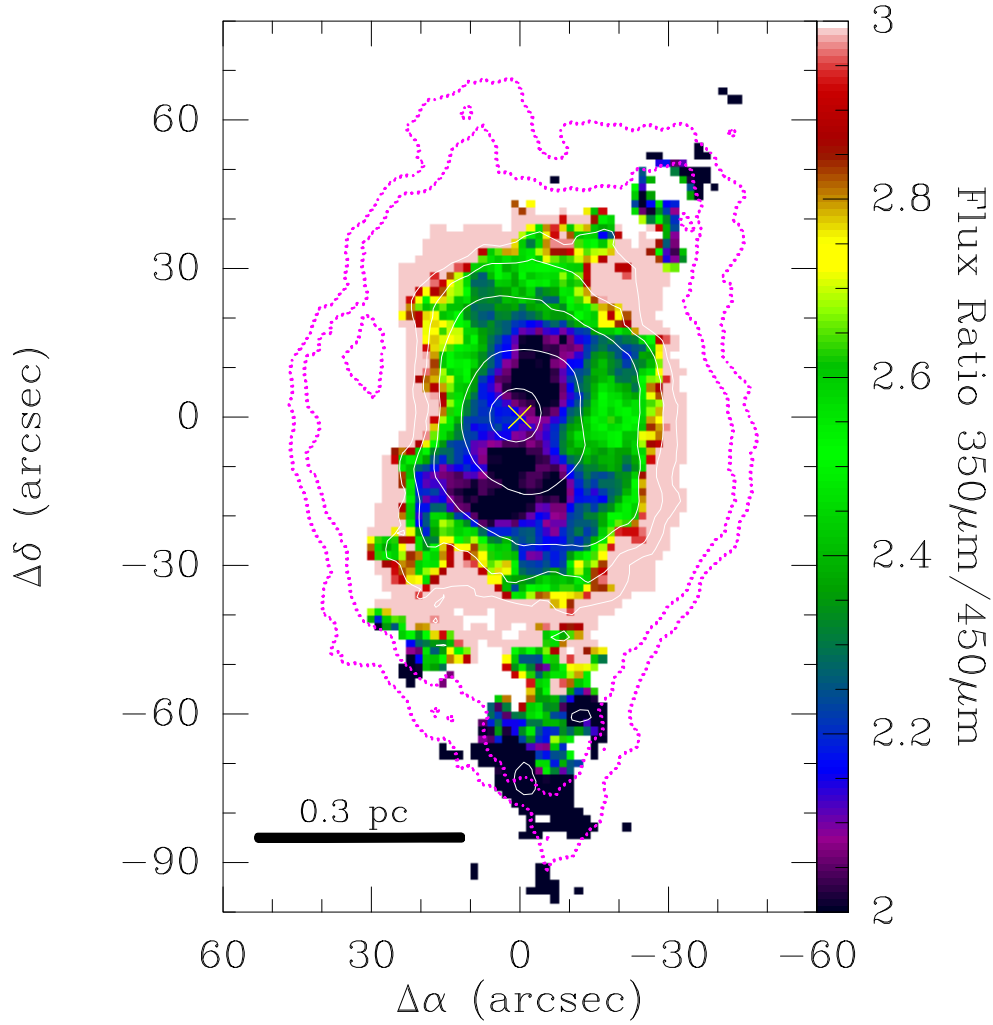


Fig. 3.—  $350\mu\text{m}/450\mu\text{m}$  flux ratio map. The  $450\mu\text{m}$  emission is drawn in white contours corresponding to  $3\sigma$ ,  $5\sigma$ ,  $9\sigma$ ,  $27\sigma$ , and  $81\sigma$ . The pink dotted contours correspond to the  $3\sigma$  and  $5\sigma$  levels of the  $350\mu\text{m}$  emission. The yellow cross marks the clump center.

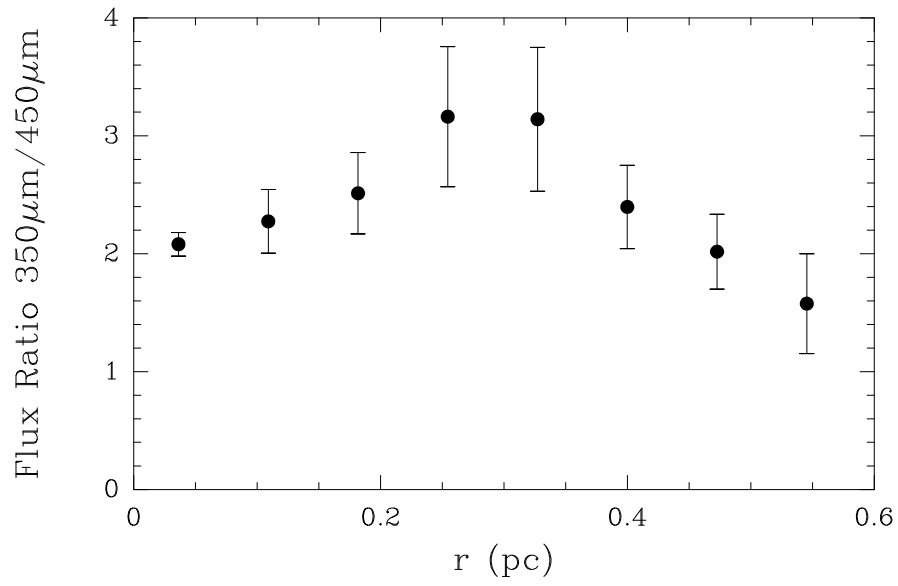


Fig. 4.— Plot of the  $350\mu\text{m}/450\mu\text{m}$  flux ratio as a function of the clump radius. The bars are the standard deviation of the ratio in each annulus.

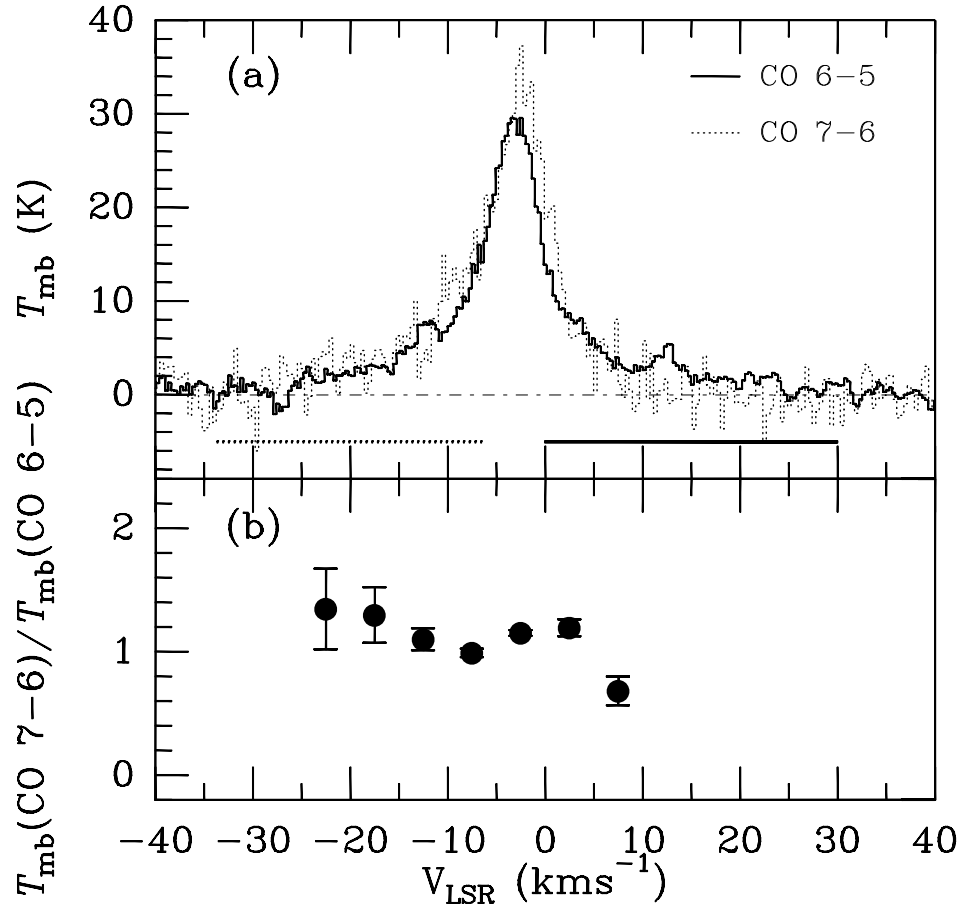


Fig. 5.— (a) CO 6–5 and 7–6 spectra observed towards the center of the clump. The solid and dashed bars under the spectra indicate the ranges of red- and blue-shifted components (see § 3.2.3). (b) Ratio of the brightness temperatures of the CO 7–6 and 6–5 emission.

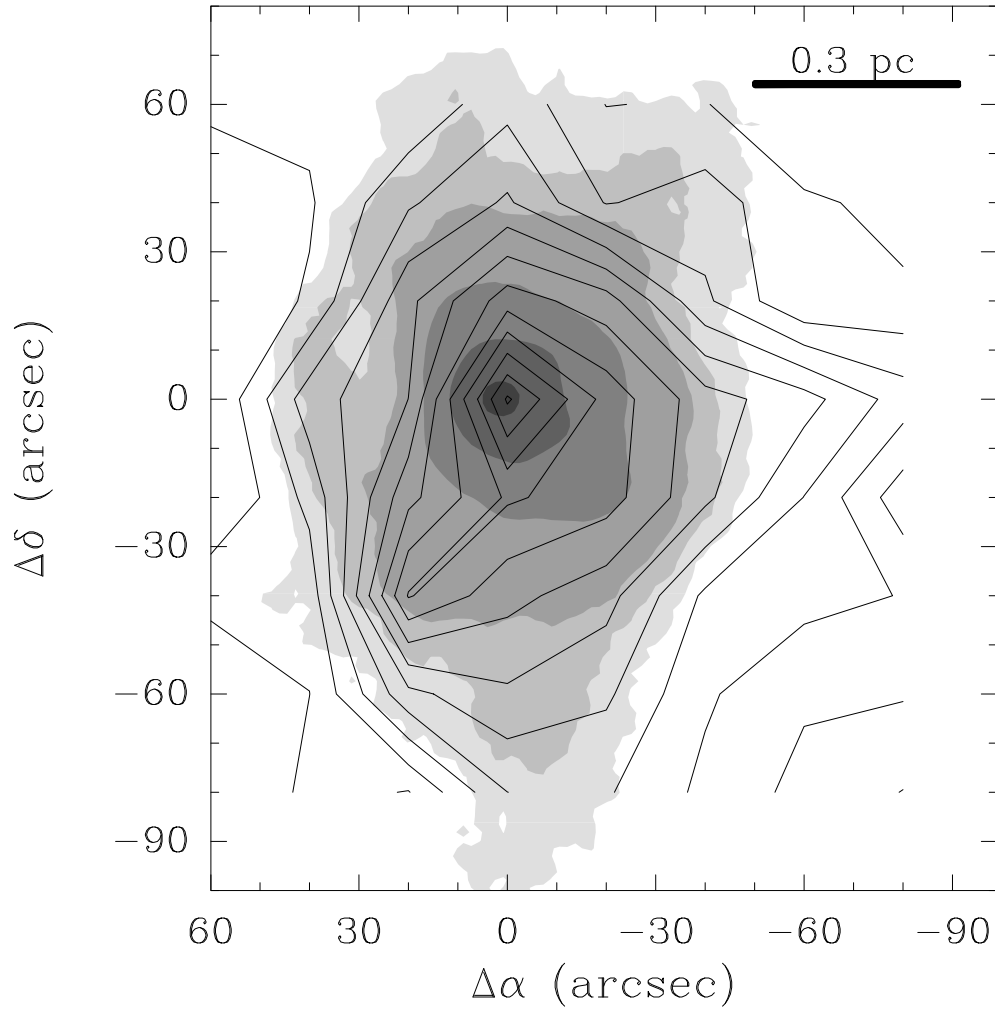


Fig. 6.— Comparison between CO 6 – 5 line emission close to the systemic velocity (black solid line contours) and the 350 $\mu\text{m}$  dust continuum emission (grey scale contours, same as Figure 1 left panel). Contours of the CO 6 – 5 map are drawn in steps of  $2\sigma$ , starting from the  $2\sigma$  level ( $10.6 \text{ K km s}^{-1}$ ).

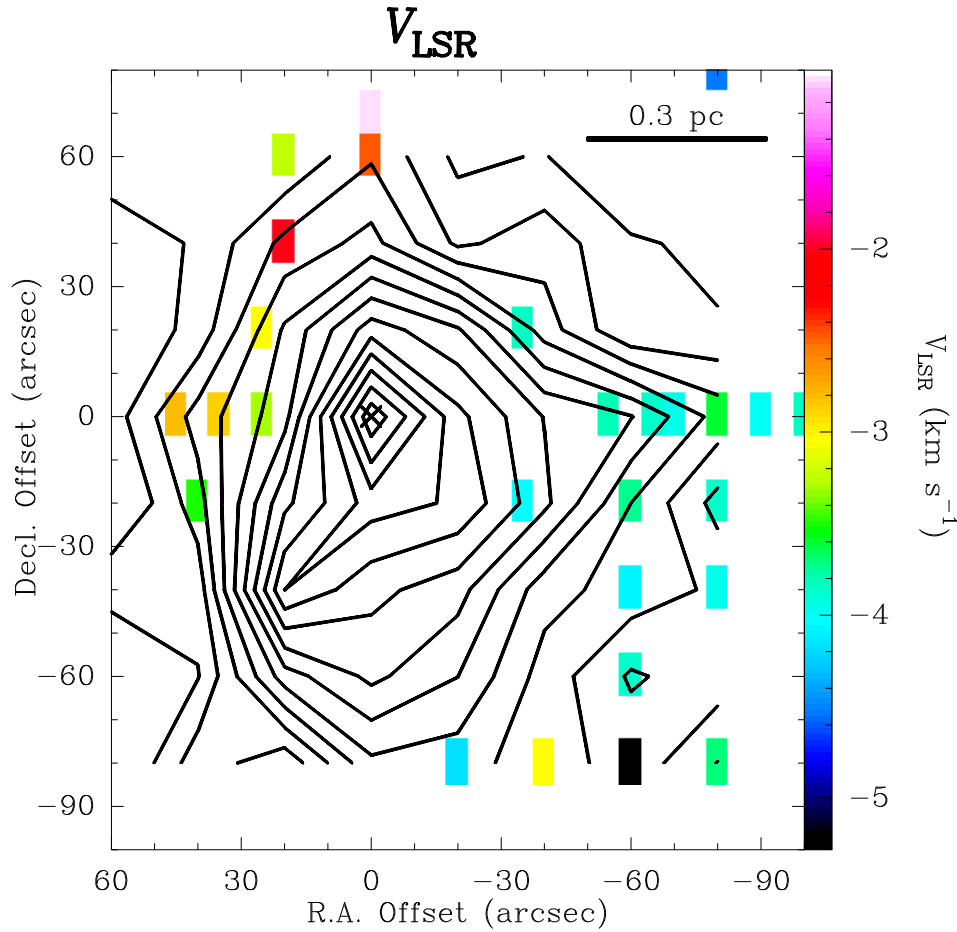


Fig. 7.— The colored pixels in the diagram represent the LSR velocities of the CO 6 – 5 narrow line-width components (contours, same as Figure 6), overlaid on the map of the CO 6 – 5 systemic velocity component (contours, same as Figure 6). The black cross denotes the clump center.

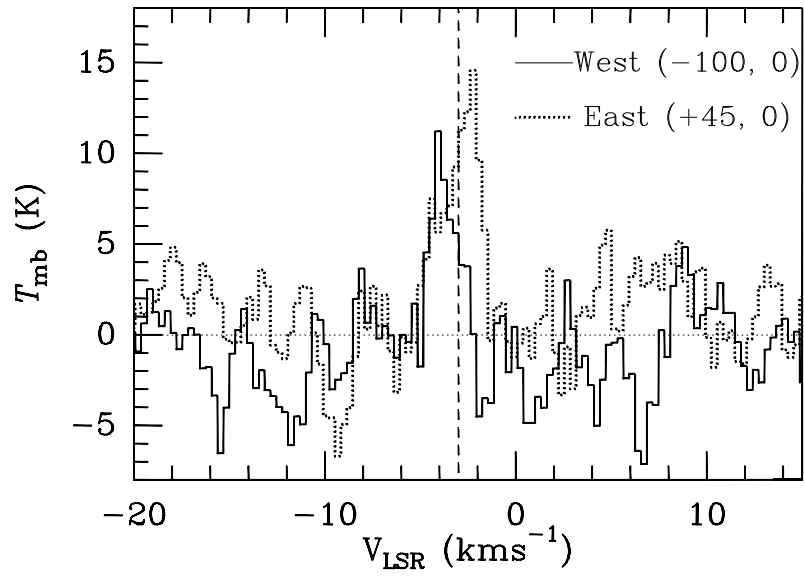


Fig. 8.— CO 6 – 5 spectra observed towards the positions at offsets (+45", 0) (east) and (+100", 0) (west) from the clump center. The dotted vertical line marks  $V_{\text{CO6-5}}$ .

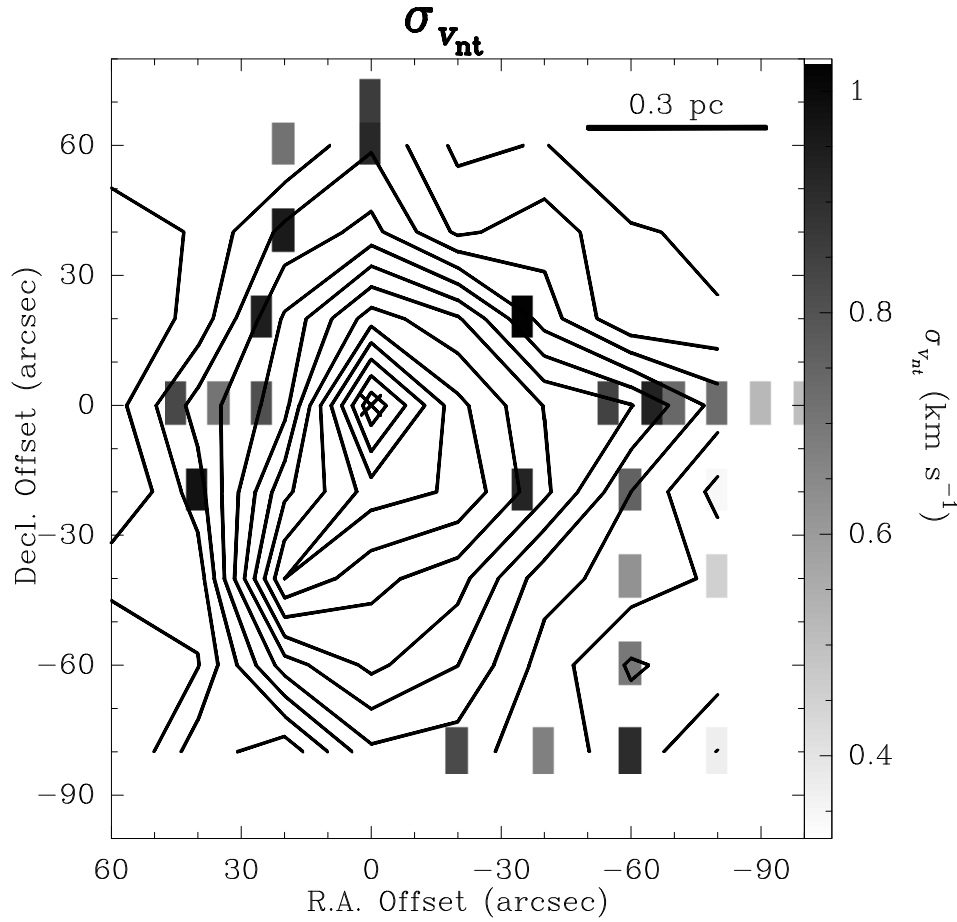


Fig. 9.— The grey scale represents the non-thermal velocity dispersion ( $\sigma_{v_{nt}}$ ) of the narrow line-width components, overlaid on the map of CO 6 – 5 systemic velocity component (contours, same as Figure 6). The black cross marks the clump center.

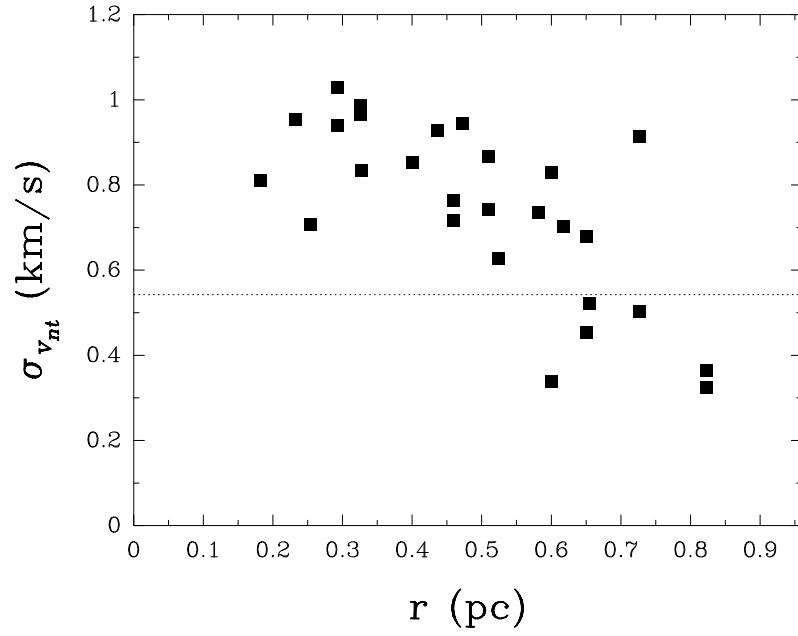


Fig. 10.— Plot of non-thermal velocity dispersion versus distance from the clump center.

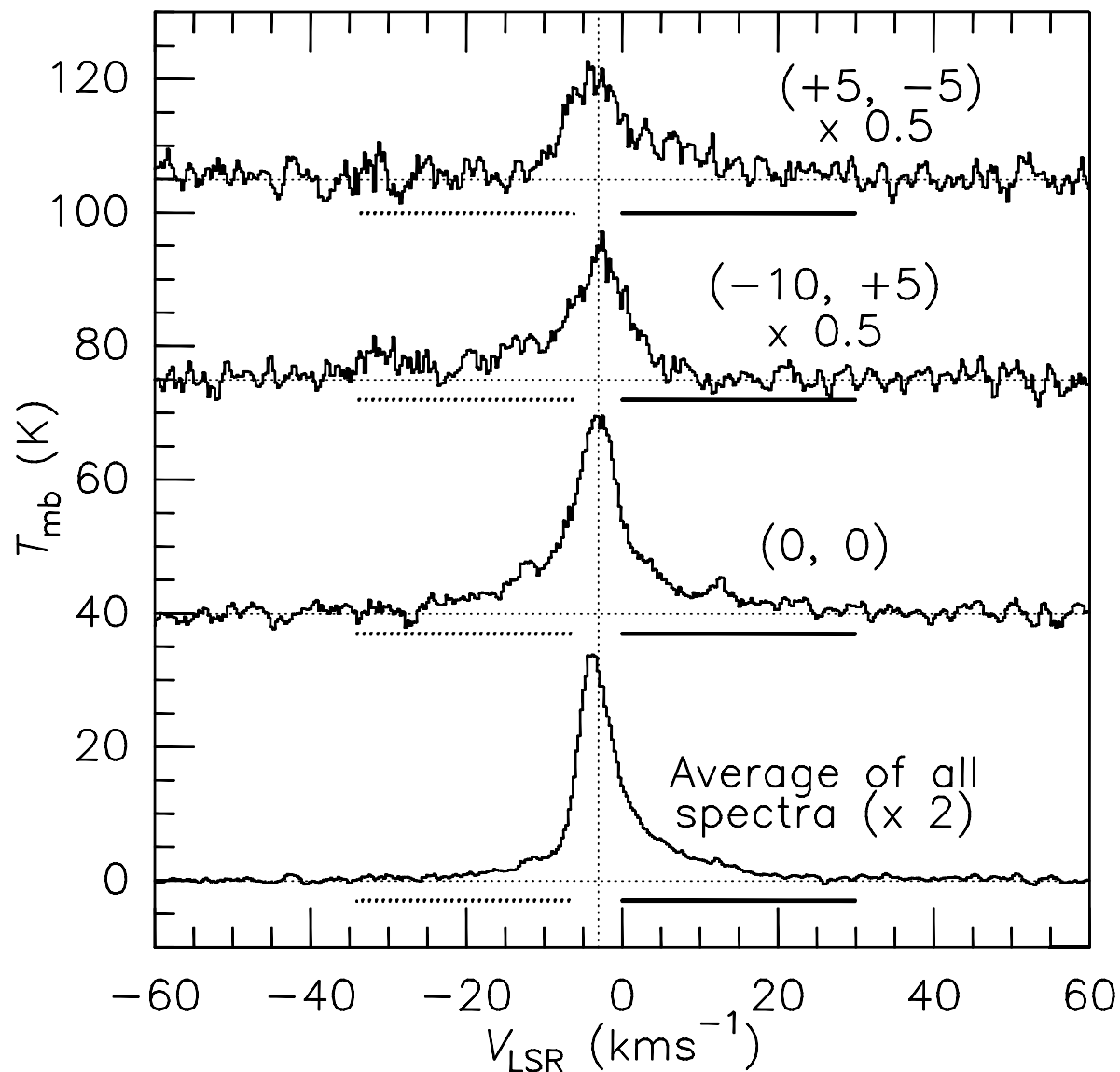


Fig. 11.— CO  $J = 6 - 5$  spectra taken towards three different positions ( $(\text{RA}_{\text{offset}}'', \text{Dec}_{\text{offset}}'')$ ) =  $(+5, -5)$ ,  $(-10, +5)$ , and  $(0, 0)$ ) and average spectrum of all spectra taken within a central area of  $1' \times 1'20''$ . The solid and dashed bars under each spectrum show the ranges of red- and blue-shifted components. The vertical dashed line is drawn at  $V_{\text{CO6-5}}$ .

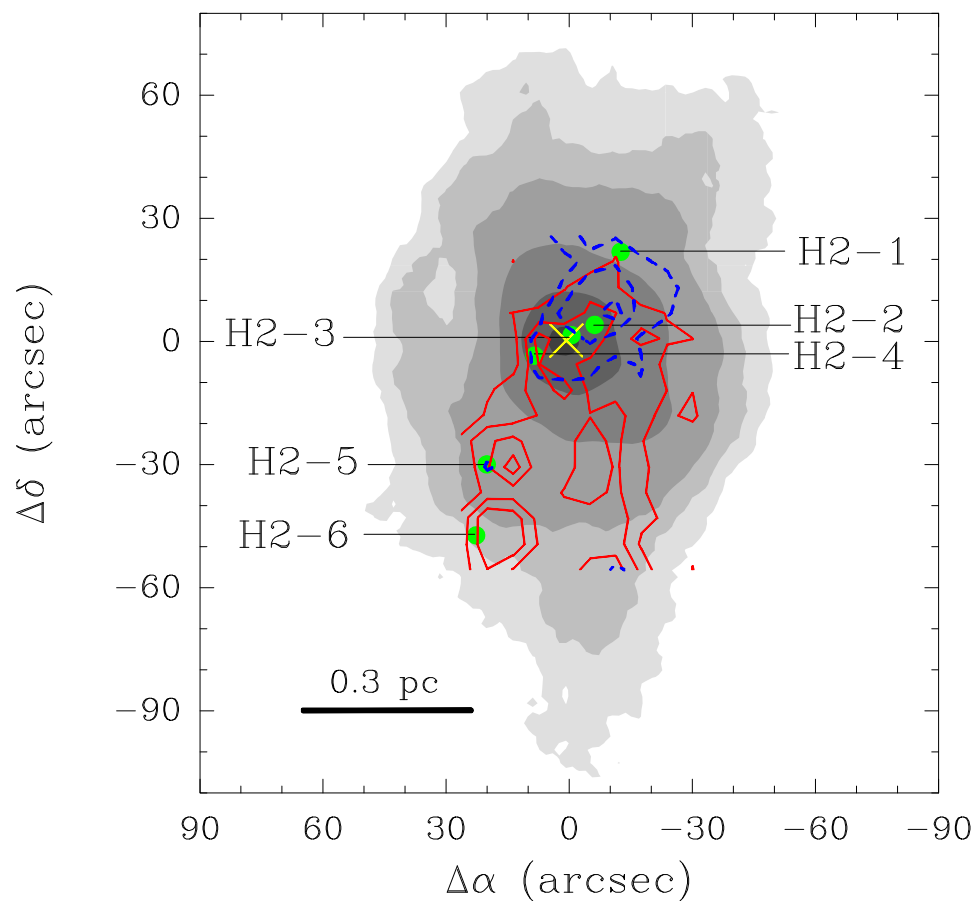


Fig. 12.— CO  $J = 6 - 5$  blue-shifted ( $-34.0 \leq V_{\text{LSR}} \text{ km s}^{-1} \leq -6.0$ , blue dashed contours) and red-shifted ( $0.0 \leq V_{\text{LSR}} \text{ km s}^{-1} \leq +30$ , red solid contours) emission superposed on the  $350\mu\text{m}$  image (same as Figure 1). Contours of the CO  $J = 6 - 5$  components are drawn in steps of  $3\sigma$ , starting from the  $3\sigma$  level ( $50 \text{ K km s}^{-1}$ ). The yellow cross marks the clump center. The shocked  $\text{H}_2$  knots (green dots) marked and numbered in the diagram are taken from Shepherd et al. (2000).

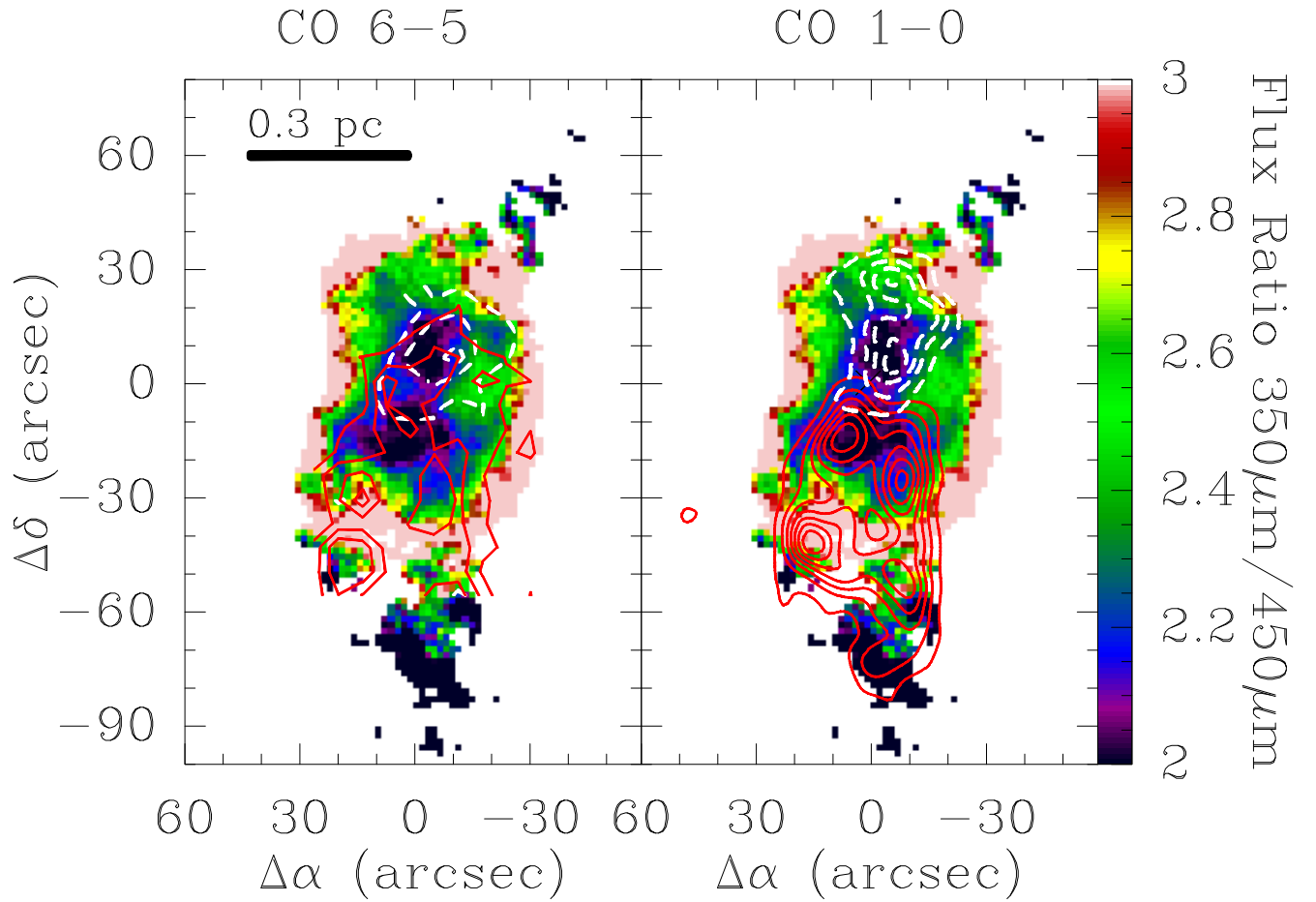


Fig. 13.— CO 6 – 5 blue- and red-shifted (left, same as Figure 12), and CO 1 – 0 blue- and red-shifted (right, same as Figure 1 of Shepherd et al. 2000) maps, superposed on the  $350/450\mu\text{m}$  flux ratio map. White dashed and red solid contours denote the blue- and red-shifted lobes respectively.